I&EC research
Industrial & Engineering Chemistry Research

Article

Cite This: *Ind. Eng. Chem. Res.* 2019, 58, 21827−21841

pubs.acs.org/IECR

Effect of Electrode Length of an Electrical Capacitance Tomography Sensor on Gas−Solid Fluidized Bed Measurements

Kai Huang,[†,‡] Shuanghe Meng,[†] Qiang Guo,[†,‡] Wuqiang Yang,[§] Tao Zhang,[†] Mao Ye,[*,†] and Zhongmin Liu[†]

[†] Dalian National Laboratory for Clean Energy and National Engineering Laboratory for MTO, Dalian Institute of Chemical Physics, Chinese Academy of Sciences, Dalian 116023, Liaoning, China

[‡] University of Chinese Academy of Sciences, Beijing 100049, Beijing, China

[§] School of Electrical and Electronic Engineering, The University of Manchester, Manchester M13 9PL, Lancashire, U.K.

Supporting Information

ABSTRACT: Electrical capacitance tomography (ECT) has been widely used in fluidized bed measurements because of the noninvasive and nonintrusive features. The successful application of ECT in fluidized bed measurements depends on the appropriate design of sensors. This paper discusses the effect of ECT sensor length on fluidized bed measurements by simulations and experiments. The sensitivity distributions in different axial positions of a sensor are compared, which shows the similarity of sensitivity distribution contours and decline of intensity along the sensor axial direction. Fluidized beds of three different diameters (45, 55, and 65 mm) are used to compare the effect of sensor electrode length on fluidized bed measurements. In each fluidized bed, five sensors with different electrode lengths are tested. The experimental results show that the sensor electrode length has significant effect on bubble detection in fluidized bed measurements, and it is recommended that the sensor electrode length should be as short as possible considering the signal-to-noise ratio constraint.

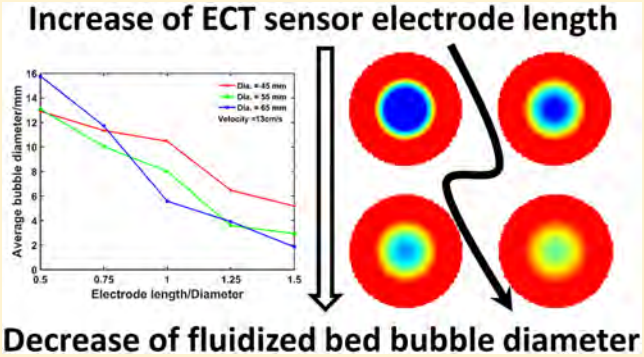

1. INTRODUCTION

1.1. Background.

Gas−solid fluidized beds are widely used in industrial processes, such as methanol-to-olefins, fluid catalytic cracking, and coal combustion.[1−3] It is important to understand the hydrodynamics of fluidized beds for the purpose of reliable design, effective scale-up, and accurate modeling. A lot of measurement methods, which can be either intrusive or nonintrusive, have been invented to investigate the gas−solid fluidized bed characteristics.[4] Various probes are often used intrusively in fluidized beds.[4] Typical examples include, but are not limited to, capacitance probes applied to measure local solid concentrations[5,6] and fiber optical probes used to monitor local solid concentrations[7] and bubble size and bubble rise velocity.[8] However, intrusive probes inevitably introduce disturbances to the gas−solid flows in the measurement region and hardly offer information in the whole cross-sectional area. The nonintrusive methods include various tomographic measurements, such as X-ray tomography, γ-ray tomography, and tomographies based on electric field and magnetic field. These methods can be used to measure the flow field of the whole cross-sectional area, despite the advantages of causing negligible disturbance to the operation of fluidized beds.[9]

Electrical capacitance tomography (ECT) is one of major tomographic techniques that has been widely used in the gas−solid fluidized bed measurements[10−18] because of the characteristics of nonintrusiveness, noninvasiveness, no radiation, fast imaging speed, withstanding harsh environments, and low cost.[19] A variety of fluidized bed characteristics, such as minimum fluidization velocity, minimum bubbling velocity, minimum slugging velocity, bubble size, bubble rise velocity, solid concentration distribution, and dominant frequency of flow fluctuations in fluidized beds, could be measured by ECT.[10−18] Recently, Li et al.[15] used a twin-plane sensor mounted on a 59 mm diameter fluidized bed, with each plane having eight electrodes with 10 mm axial length, to evaluate bubble size. They first used a hollow phantom with different diameters to estimate the suitable cutoff value, to evaluate bubble diameters, and to compare the results with correlations. They[16] also compared ECT measurements with pressure fluctuation measurements in bubbling gas−solid fluidized beds. They found that the two measurement

Received: July 20, 2019
Revised: October 30, 2019
Accepted: November 1, 2019
Published: November 1, 2019

DOI: 10.1021/acs.iecr.9b03988
Ind. Eng. Chem. Res. 2019, 58, 21827−21841

techniques provided consistent results, and ECT tended to be more reliable with respect to estimating bubble rise velocity. Agu et al.[13,14,17,18] used a twin-plane sensor, in which each plane is composed of 12 electrodes, to study fluidization in a 10.4 cm diameter fluidized bed. They[13] first put forward methods to determine the onsets of incipient, bubbling, and slugging fluidization. Then, they[14,17] studied bubble characteristics in fluidized beds using a cutoff value of 0.2 (i.e., solid concentration) to identify bubbles and proposed models to predict bubble diameter, volumetric bubble flux, transition velocity from bubbling to slugging bed, bubble rise velocity, bubble frequency, and bed expansion. They also[18] studied the effect of particle properties and bed height on bubble characteristics of fluidized beds. Chandrasekera et al.[12] considered the sharp transition between bubble and emulsion phases and proposed a new algorithm that penalizes the total variation of images to reconstruct images with sharp boundary. They used a 12-electrode sensor with 70 mm sensor length which was mounted on a 50 mm diameter fluidized bed to measure bubble size. They used the new algorithm and obtained more accurate results. Makkawi and Wright[10] used a two-plane ECT sensor with each electrode length of 38 mm, which was mounted on a 15 cm diameter fluidized bed to study fluidized bed regime transitions. They analyzed solid concentration profile, average solid concentration with its standard deviation, and dominant frequency obtained from a solid concentration series by fast Fourier transform (FFT) algorithm and identified single bubble, slugging, turbulent, and fast fluidization regimes with respect to the increase of superficial velocity. Qiu et al.[11] also used a two-plane ECT sensor with each electrode length of 6 cm, which was mounted on the bottom region of three different diameter (i.e., 10, 12, and 15 cm) circulated fluidized beds to study fluidized bed characteristics and regime transitions. They also studied the effect of ratio of static bed height to diameter on fluidized bed characteristics.

It can be seen that ECT could be used to measure fluidized bed characteristics, but the ECT sensors used have different constructions. In particular, the electrode length reported in the studies mentioned above is not consistent with each other. The effect of sensor electrode length on fluidized bed measurements has not been studied so far. Therefore, the aim of this paper is to investigate the effect of ECT electrode length on the measurement of hydrodynamic characteristics in fluidized beds, especially the bubble size, and find the optimal design of the ECT sensor when applied to fluidized bed measurements.

1.2. Previous Work of ECT Sensor Design. A typical ECT system consists of a multielectrode sensor, sensing electronics, and a computer for hardware control, data processing, and image reconstruction algorithms.[20] For a particular application, an ECT sensor needs to be designed according to the shape and size of the object under investigation. In the past, researchers studied the sensor type, the number of electrodes, the electrode length, and the electrode-to-gap ratio, that is, the ratio of electrode coverage to gap coverage in sensor cross section, for ECT sensor design.[21−25] Hua et al.[21] analyzed three different types of sensors using a three-dimensional (3D) finite element method and concluded that it was appropriate to use an ECT sensor with earthed ring electrodes when permittivity distribution along the axial direction of measurement zone was not consistent. Considering the chaotic behavior of gas and solids in a fluidized bed, that is, solid concentration along the axial direction of the fluidized bed is changing all the time, it is beneficial to use an ECT sensor with earthed ring electrodes. For designing an ECT sensor used for fluidized bed measurements, though some researchers have suggested the number of electrodes and electrode-to-gap ratio,[22,25] the effect of electrode length on fluidized bed measurements has not been reported so far.

Hua et al.[21] studied the effect of ratio of electrode length to sensor diameter on ECT sensing field. They found that increasing the ratio of electrode length to sensor diameter could reduce the difference between the sensing fields simulated by two-dimensional (2D) model and that by 3D model but did not consider the influence on final measurement results. Peng et al.[23] also simulated the effect of electrode length of a square ECT sensor on the measurements, by which they studied the sensitivity distributions in different axial positions of a sensor and showed that contours of sensitivity distribution in different axial positions were similar to each other. They also compared the capacitance vectors of three same phantoms measured by sensors with different electrode lengths and recommended that the optimal length of the electrode should be the same as the diameter or width of an ECT sensor. However, in the study, they did not consider the nonuniform permittivity distribution along the axial direction of the measurement zone, and the reconstructed images of the same nonuniform permittivity distribution measured by the sensor with different electrode lengths were not compared. Similarly, Sun and Yang[24] studied the fringe effect of the sensor with different electrode lengths. They concluded that a sensor with longer electrodes and end guards could reduce the fringe effect. However, they did not discuss the effect of sensor electrode length on axial inconsistent permittivity measurements.

In this paper, therefore, the effect of ECT sensor electrode length on fluidized bed measurements is experimentally studied by use of three fluidized beds with different diameters (i.e., 45, 55, and 65 mm). For each fluidized bed, five sensors with different electrode lengths are fabricated. Simulation studies are conducted to understand the change of sensitivity distribution along the axial direction of the sensor and the effect of axial position on ECT measurements in the fluidized bed. In addition, a phantom is also placed at the center of different length sensor to experimentally study the effect of electrode length on bubble detection in fluidized beds.

2. ECT AND IMAGE RECONSTRUCTION ALGORITHMS

In ECT measurements, the measured capacitance vector is used to reconstruct the permittivity distribution as a representation of the material distribution over a cross section of a fluidized bed.[20] The relationship between the capacitance vector and material distribution (i.e., solid concentration distribution in a fluidized bed) is commonly approximated as[20]

$$\lambda = Sg \tag{1}$$

where λ is the normalized capacitance vector with a dimension of 66 × 1 for a 12-electrode sensor,[26] g is the normalized permittivity vector (i.e., solid concentration distribution in a fluidized bed) with a dimension of 3228 × 1 in a circular sensor, and the entry number is the same as the number of pixels in the measurement zone. We found that the pixel number does not influence the reconstructed permittivity distribution, but a higher pixel number could lead to smoother images of gas−solid distributions. The procedure on how to divide the measurement zone into 3228 pixels, as well as the comparison between the reconstructed images obtained from the same normalized capacitance vector in different pixels, could be seen in Supporting Information 1. S is the normalized sensitivity distribution matrix with a dimension of 66 × 3228.

The sensitivity distribution matrix S^* represents variation of capacitance of each electrode pair in response to a perturbation of the permittivity distribution.[27] Therefore, $S_{ij}^*(x,y)$ defines the sensitivity between the i−j electrode pair at the location of pixel $p(x,y)$, where (x, y) represents the coordinate of pixel center, which is commonly obtained from electric fields as given by

$$S_{ij}^{*}(x, y) = -\iint_{p(x,y)} \frac{E_i}{V_i}\cdot\frac{E_j}{V_j}\,\mathrm{d}x'\,\mathrm{d}y' \tag{2}$$

where $p(x,y)$ represents the pixel with center coordinate (x, y). E_i and E_j are electric field strengths inside the sensing domain $A(x',y')$ when excitation voltages V_i and V_j are applied to the ith and jth electrodes, respectively, while other electrodes are used as detection electrodes. The normalized sensitivity matrix S is then calculated as

$$S_{mn} = \frac{S_{mn}^*}{\sum_{n=1}^{N} S_{mn}^*} \qquad (m = 1{:}\ M,\ \ n = 1{:}\ N) \tag{3}$$

where S_{mn} and S_{mn}^* are entries in the mth row and nth column of S and S^*, respectively, m is the mth electrode pair, n is the nth pixel, M is the number of electrode pairs (i.e., 66 in a 12-electrode sensor system), and N is the effective number of pixels in the circular sensor, which is 3228. Note that the sensitivity distribution matrix (S^*) is calculated based on a vacuum permittivity distribution, although it actually changes with the permittivity distribution. The normalized capacitance is computed by following equation

$$\lambda = \frac{C - C_{\mathrm{L}}}{C_{\mathrm{H}} - C_{\mathrm{L}}} \tag{4}$$

where C is the measured capacitance, C_{L} is the capacitance of the corresponding electrode pair in low calibration procedure, and C_{H} is the capacitance of the corresponding electrode pair in high calibration procedure.

Image reconstruction algorithms play an important role in ECT measurements. In this work, the projected Landweber iteration algorithm with an optimal step length is used to obtain the permittivity distribution.[20,28,29]

$$\widehat{g_0} = S^{\mathrm{T}}\lambda \tag{5}$$

$$\widehat{g_{k+1}} = P[\widehat{g_k} - \alpha S^{\mathrm{T}}(S\widehat{g_k} - \lambda)] \tag{6}$$

$$P[x] = \begin{cases} 0 & \text{if } x < 0 \\ x & \text{if } 0 \le x \le 1 \\ 1 & \text{if } x > 1 \end{cases} \tag{7}$$

where

$$\mathrm{e}^{(k)} = \lambda - S\widehat{g_k} \tag{8}$$

$$\alpha = \frac{\left\|S^{\mathrm{T}}\ \mathrm{e}^{(k)}\right\|^2}{\left\|SS^{\mathrm{T}}\ \mathrm{e}^{(k)}\right\|^2} \tag{9}$$

The initial estimation $\widehat{g_0}$ is obtained based on the linear back-projection algorithm,[20] which is shown in eq 5. In eq 8, e is the vector of errors between the measured and calculated capacitance. The optimal step length α is computed by eq 9 according to Liu et al.[28] P is the function operator defined in eq 7. One of the drawbacks of the projected Landweber iteration algorithm is its semiconvergence; therefore, it is necessary to choose an appropriate number of iterations. Following Guo et al.,[29] some phantoms obtained from the computational fluid dynamics (CFD) simulations of a fluidized bed are used as references to assess the performance of the algorithm with different iteration numbers. Figure 1 shows the effect of iteration numbers on solid concentration measurements for 16 randomly selected phantoms. Solid concentration is calculated by averaging the normalized permittivity and multiplying the solid concentration of a packed bed as given by

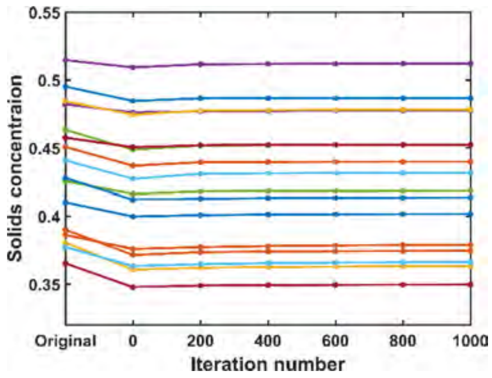

Figure 1. Effect of iteration number on solid concentration measurements for 16 randomly selected phantoms.

$$\beta = \theta\cdot\hat{g} = \theta\cdot\frac{\sum_{i=1}^{N}\widehat{g_i} \times s_i}{\sum_{i=1}^{N} s_i} \tag{10}$$

where β is the solid concentration, s is the area of each image pixel, and θ is the solid concentration of a packed bed, which is set to 0.63 in this work.

In the horizontal axis of Figure 1, tag "Original" represents the solid concentrations directly obtained from fluidized bed simulations. It can be seen from Figure 1 that when the number of iterations is more than 200, the solid concentration has little change. Therefore, 200 is chosen as the number of iterations in the following analyses.

3. SIMULATION STUDY

In the simulation studies, sensitivity distributions along the axial direction of an ECT sensor are investigated. Also, the effect of electrode length on ECT measurements is studied by placing the same phantom in different axial positions of the sensor and at the center of sensors of different lengths.

3.1. Sensor Structure. Figure 2 shows the structures of ECT sensors in the simulation studies, and the same structures of ECT sensors are used for corresponding experimental studies. Note that three different columns (i.e., 45, 55, and 65 mm inner diameter) are constructed, and the wall thickness of the columns are all 2 mm. The configuration parameters of the sensors are shown in Table 1. Five sensors with different relative electrode lengths (0.5, 0.75, 1, 1.25, and 1.5) are simulated for each column. Here, the relative electrode length

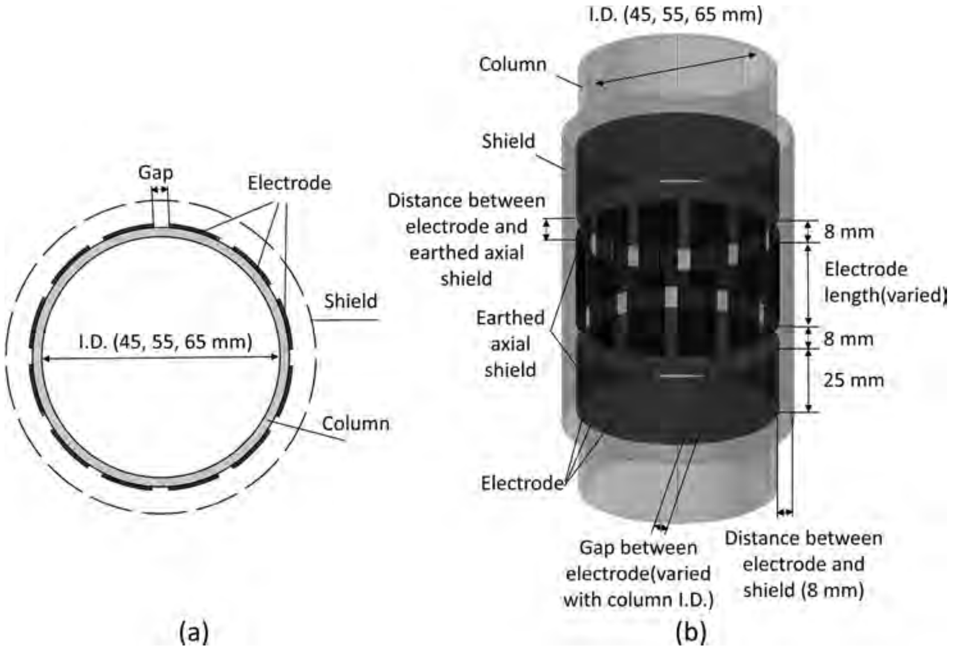

Figure 2. ECT sensor configurations. (a) Cross-sectional view. (b) Overall view.

Table 1. Parameters of ECT Sensor Configurations

column inner diameter	65, 55 and 45 mm
column thickness	2 mm
electrode number	12
electrode thickness	0.5 mm
electrode-to-gap ratio	4
relative electrode length	0.5, 0.75 1, 1.25 and 1.5
distance between earthed screen and electrodes	8 mm
distance between shield screen and electrodes	10 mm
shield length	180 mm

is defined as the ratio of electrode length to the corresponding column inner diameter. When the column inner diameter and electrode-to-gap ratio are specified, the width of the electrode is obtained.

During simulations, all the parameters are kept the same except for the electrode length and column size. The electric fields obtained from simulations with different grid resolutions are compared and an appropriate grid size is identified. The cross section in the center of the electrode is set as $z = 0$ plane. The positive direction is set upward. Considering the symmetry of sensitivity distributions about $z = 0$ plane, only the upper axial section of the sensor is studied, which is divided into several slices in the axial direction of the sensor regarding the electrode length. In addition, simulations are conducted in a 2D model with the same structure as shown in Figure 2a.

3.2. Mathematical Basics of Sensor Simulation. The governing equation used in the sensor simulations is the Laplacian equation described as[23]

$$\nabla\cdot[\varepsilon(x, y, z)\nabla\phi(x, y, z)] = 0 \tag{11}$$

the relevant boundary condition is

$$\phi(x, y, z) = \begin{cases} V & (x, y, z) \in \Gamma_i \\ 0 & (x, y, z) \in \Gamma_k(k \neq i) \text{ or } (x, y, z) \in \Gamma_S \end{cases} \tag{12}$$

where Γ_i is the excitation electrode, Γ_k is the detection electrode, and Γ_s stands for the shield and earthed axial shield electrodes. The capacitance between the ith and jth electrodes is computed as

$$C_{ij} = \frac{q(\Gamma_j)}{V} = -\frac{1}{V}\int_{\Gamma_j} \varepsilon(x, y, z)\nabla\phi^{(i)}(x, y, z)\cdot \mathrm{d}\Gamma_j \tag{13}$$

where $q(\Gamma_j)$ is the quantity of electric charge in the Γ_j electrode when the Γ_i electrode is excited.

3.3. Numerical Results. The simulation study is first carried out to explore the difference of sensitivity distributions in different axial positions of the sensor. Sensitivity distribution reflects the sensitivity of electrode pair capacitance variation over permittivity perturbation in pixel (2D) or voxel (3D) inside the measurement zone from the definition as shown below[27]

$$S_{ij}(k) \approx \frac{\Delta C}{(\varepsilon_H - \varepsilon_L)\cdot s_k} = \frac{C_{ij}(k) - C_{ij}^L}{\varepsilon_H - \varepsilon_L}\cdot\frac{1}{s_k} \tag{14}$$

where $S_{ij}(k)$ is the sensitivity of the i–j electrode pair in the kth pixel (or voxel), $C_{ij}(k)$ is the capacitance when pixel (or voxel) k has high permittivity ε_H and the rest has low permittivity ε_L, and s_k is the area (or volume) of pixel (or voxel) k. Therefore, the effect of axial position of cross section of the sensor on electrode pair measurements could be obtained by comparing the sensitivity distributions along the axial direction of the sensor. Each cross section is divided into 3228 pixels and sensitivity distribution based on these pixels is calculated by eq 2. Note that we do not compare the normalized sensitivity distribution in this case because it eliminates electric field intensity in different axial positions of sensor according to the definition shown in eq 3.

In this work, sensitivity distribution similarities between different axial positions of sensor are quantitatively compared using the parameter of correlation coefficient. The correlation coefficients of sensitivity distribution in different positions are computed by

$$r = \frac{\sum_{m=1}^{M}\sum_{n=1}^{N}(S1_{mn}^{*} - \overline{S1^{*}})(S2_{mn}^{*} - \overline{S2^{*}})}{\sqrt{\sum_{m=1}^{M}\sum_{n=1}^{N}(S1_{mn}^{*} - \overline{S1^{*}})^{2}(S2_{mn}^{*} - \overline{S2^{*}})^{2}}} \tag{15}$$

where $S1^*$ and $S2^*$ are the matrixes representing the original sensitivity distributions in different cross sections, $\overline{S1^*}$ and $\overline{S2^*}$ are the average over all elements in the corresponding matrix, respectively, and r is the correlation coefficient between $S1^*$ and $S2^*$, which takes all electrode pairs into account.

The sensitivity distribution obtained by the 2D model, as shown in Figure 2a, is used as the base, and the sensitivity distributions in different axial positions are compared to that of the 2D model.

Figure 3 shows the correlation coefficients between the sensitivity distributions of different axial positions of the sensor with different electrode lengths and that of the 2D model in a 55 mm inner diameter column. Two vertical lines are used to distinguish the electrode edge and the lower edge of the earthed screen. It shows that the correlation coefficients approach 1.0 when the axial position of the sensor does not exceed the electrode edge irrespective of the electrode length, indicating that the sensitivity distribution contours are similar. However, the similarity decreases when the axial position of the sensor becomes out of the electrode edge.

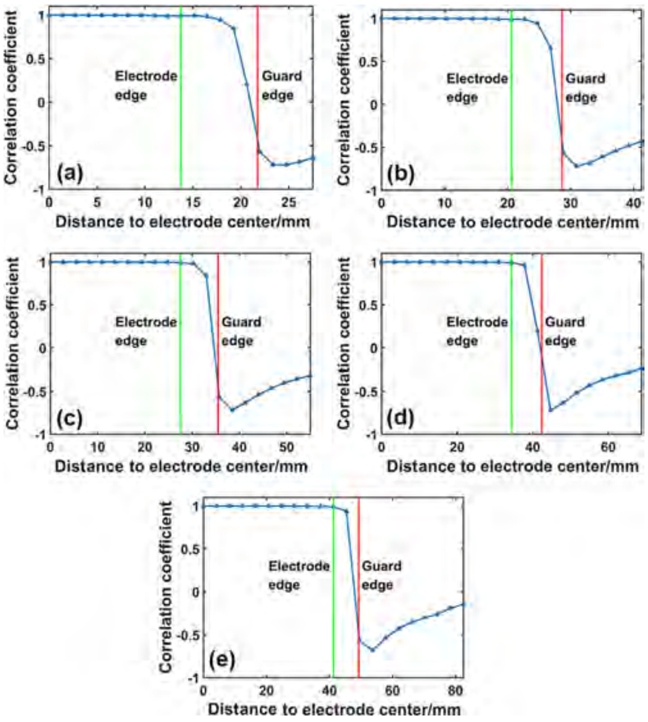

Figure 3. Correlation coefficients between the sensitivity distributions of different axial positions of the sensor with different electrode lengths and that of the 2D model in the 55 mm diameter column. (a) 27.5 mm, (b) 41.25 mm, (c) 55 mm, (d) 68.75 mm, and (e) 82.5 mm.

The sensitivity distributions of the opposite electrode pair in different axial positions of the sensor with an electrode length of 55 mm in the 55 mm diameter column are shown in Figure 4. It shows that the contours of sensitivity distributions are similar to each other in different planes when the axial positions are within the electrode edge. Similar results are also obtained for the columns with inner diameters of 45 and 65 mm.

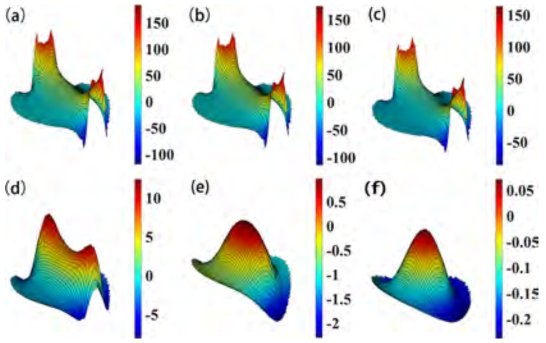

Figure 4. Sensitivity distributions of opposite pair in different axial planes for the 55 mm diameter column with an electrode length of 55 mm. (a) $z = 0$, (b) $z = 11$ mm, (c) $z = 22$ mm, (d) $z = 33$ mm, (e) $z = 44$ mm, and (f) $z = 55$ mm.

As shown in Figures 3 and 4, sensitivity distribution contours are similar to each other; therefore, an index called sensitivity distribution intensity is used to quantify the intensity of sensitivity distribution in different sensor axial positions, which is expressed by

$$\text{Sensitivity distribution intensity} = \frac{\sum_{i=1}^{M}\sum_{j=1}^{N}(|S1_{ij}^{*}|/|S2_{ij}^{*}|)}{M \times N} \tag{16}$$

It can be seen that the sensitivity distribution intensity in eq 16 actually compares the intensity of original sensitivity distribution in corresponding pixels. Figure 5 shows the original sensitivity distribution intensities in different relative axial positions of sensor with different electrode lengths in the 55 mm diameter column. The sensitivity distribution in the $z = 0$ plane is used as the reference and the relative distance to electrode center is obtained by dividing the distance to electrode center by the corresponding inner diameter. Although the correlation coefficients outside the electrode decrease quickly, the sensitivity distribution intensity can reflect the effect of different sensor axial positions on capacitance measurements according to eq 14.

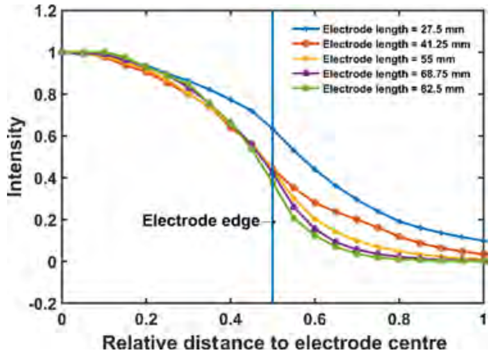

Figure 5. Intensities of sensitivity distribution in different relative axial positions of different sensors in the 55 mm diameter column.

Figure 5 shows that the sensitivity distribution intensity is the maximum in the electrode center plane and decreases with the increase of distance to the electrode center and finally approaches zero in a plane relevant to the electrode length and normally outside the electrode edge.

The effect of sensor axial position on ECT measurements is further studied by placing the same phantom in different axial positions of a sensor. A 30 mm diameter sphere with the permittivity identical to the material used for high-calibration procedure is placed at the center of different axial positions of the sensor with an electrode length of 55 mm in the 55 mm diameter column. Capacitance vectors are measured and shown in Figure 6a. It shows that the normalized capacitance vectors decrease with the increase of distance between the phantom center and electrode center. Figure 6b shows the reconstructed images of the phantom in different axial positions (the bottom edge of the electrode is set as $z = 0$ plane). It can be seen that the reconstructed image shrinks with the increase of distance between the electrode center and phantom center and finally disappears, which is related to the decrease of sensitivity distribution intensity along the sensor axial position as shown in Figure 5.

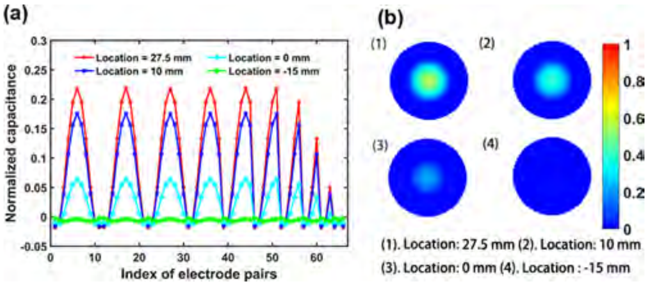

Figure 6. In a sensor with an electrode length of 55 mm in the 55 mm diameter column: (a) normalized capacitance vectors, (b) reconstructed images of the same phantom at the center of cross sections in different positions of the sensor.

Simulation is also conducted by placing the same phantom at the center of the sensor with different electrode lengths to show the effect of sensor electrode length on ECT measurements. The 55 mm diameter column is filled with the material that is used in the high-calibration procedure. Different electrode lengths (i.e., 27.5, 41.25, 55, 68.75, and 82.5 mm) of the sensor are simulated. The phantom whose diameter is 27.5 mm and permittivity is the same as that set in the low-calibration procedure (i.e., empty) is used to simulate a bubble in the fluidized bed. Figure 7a,b shows the reconstructed images and average gray levels of phantom at the center of the sensor with different electrode lengths, respectively. The average gray level is used to describe the effect of sensor electrode length on bubble detection. The computation follows eq 17, which is similar to the computation of solid concentration in eq 10 without multiplying the solid concentration of the packed bed.

$$\hat{g} = \frac{\sum_{i=1}^{N} \widehat{g_i} \times s_i}{\sum_{i=1}^{N} s_i} \qquad (17)$$

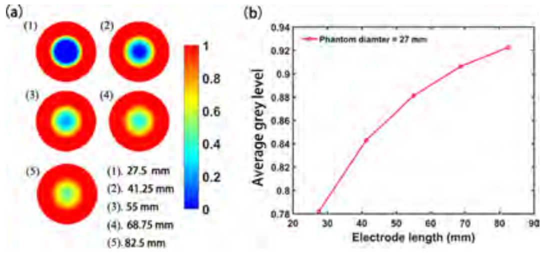

Figure 7. (a) Reconstructed images, (b) average gray level of a bubble phantom at the center of the sensor with different electrode lengths in the 55 mm diameter column.

Specifically, Figure 7b shows that the average gray level is increasing with sensor electrode length, which indicates that bubble detection becomes more difficult with the increase of sensor electrode length. As expected, the ability to detect bubbles decreases with the increase of electrode length of sensor, as shown in Figure 7a.

From the above discussion, it can be argued that the sensor electrode length is an important parameter that influences ECT measurements. Because of the chaotic motion of gas and solids in gas–solid fluidized bed, it is important to compare the effect of sensor electrode length on fluidized bed measurements for optimizing ECT sensor design.

4. EXPERIMENTAL STUDY

4.1. Experimental Setup.

An AC-based ECT system[20] is used in the following experiments. The sensing electronics is made by ECT Instruments Ltd. in the UK.[20] As shown in Figure 8a, three cylindrical fluidized beds with different inner diameters (i.e., 45, 55, and 65 mm) made by glass are used. The fluidized bed column is 1 m high and 2 mm thick. The height of static bed is set to 220 mm for all experiments. In the fluidized bed columns, porous polypropylene plates with a pore diameter of about 70 μm and a thickness of 10 mm are used as a gas distributor. The fluidized bed pressure drop and distributor pressure drop are measured. Preliminary results show that the ratio of distributor pressure drop to fluidized bed pressure drop is about 0.56 in the minimum fluidization state for fluidized beds with different diameters. As we keep the same static bed height in the experiments, this actually indicates the uniform characteristic of distributor according to the work of Sathiyamoorthy and Horio.[30] The experimental sensors are consistent with those set up in the simulation study as shown in Table 1. The axial center of the ECT sensor consisting of 12 electrodes is located in the plane of 150 mm high above the distributor. As shown in Figure 8b,c, the relative electrode lengths relative to fluidized bed inner diameter are set to 0.5, 0.75, 1, 1.25, and 1.5; the earthed axial shield length is set to 25 mm; and the distance between it and the electrode edge is set to 8 mm, and other parameters

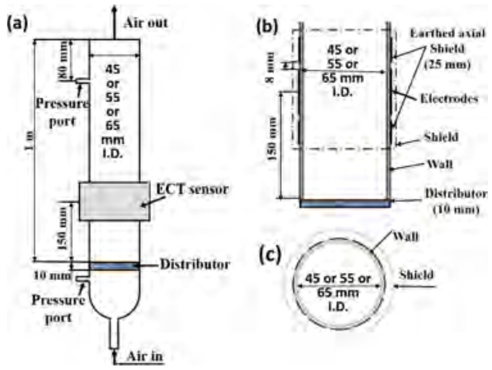

Figure 8. (a) Schematic illustration of fluidized beds. (b) Vertical view of the electrode sensor. (c) Cross-sectional view of the electrode sensor.

can be found in Table 1. Alumina is used as the fluidizing medium, with a Sauter diameter of 295 μm (Malvern Mastersizer), as shown in Figure 9, and other properties are shown in Table 2. All experiments were conducted at the same superficial velocities, spanning from fixed bed to slugging bed and even to turbulent bed.

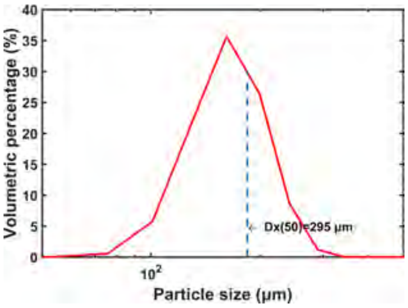

Figure 9. Particle size distribution.

4.2. ECT Sensor and Measurement Procedure.

The signal-to-noise ratio (SNR) is first checked before the experiments because the capacitance measurements are proportional to electrode length, and thus, the measurement accuracy must be guaranteed when the electrode length decreases. SNR is defined as[31]

$$\mathrm{SNR}_m = 20\log_{10}\sqrt{\frac{\sum_{i=1}^{Q}\lambda_{mi}^{\ 2}}{\sum_{i=1}^{Q}(\lambda_{mi}-\overline{\lambda_m})^2}} \tag{18}$$

$$\overline{\mathrm{SNR}} = \sum_{m=1}^{M}\mathrm{SNR}_m/M \tag{19}$$

where λ_{mi} is the relative capacitance of the ith frame of mth electrode pair, $\overline{\lambda_m}$ is the average normalized capacitance of all frames of the mth electrode pair, Q is the number of frames (i.e., 20 000), SNR_m is the SNR of the mth electrode pair, and $\overline{\mathrm{SNR}}$ is the average SNR of all electrode pairs. The benchmark of SNR is identified to determine whether the measurement accuracy is sufficient. The procedure to determine the benchmark is described below. In total, 16 sets of randomly chosen measurement data (i.e., normalized capacitance) were first chosen and added with white Gaussian noise according to the SNR level from 10 to 70 dB in a step of 2 dB. Then, the normalized permittivity distributions were reconstructed from normalized capacitance vectors with different SNR levels by the same algorithm. After that, the normalized permittivity distributions reconstructed from different SNR levels were compared with the noise-free results. Correlation coefficients were used to identify the SNR benchmark. Figure 10 shows the variation of correlation coefficients for 16 randomly chosen measurements. It can be seen that all correlation coefficients are higher than 0.9987 when the SNR is higher than 42 dB. In this regard, the effect of noise on measurement results could be ignored. Thus, an SNR of 42 dB could be considered as the benchmark, which normally has a correlation coefficient higher than 0.9987. Supporting Information 2 lists the lowest correlation coefficients of the 16 randomly chosen data with different SNR levels, which can be used as a reference to evaluate the sensor performance.

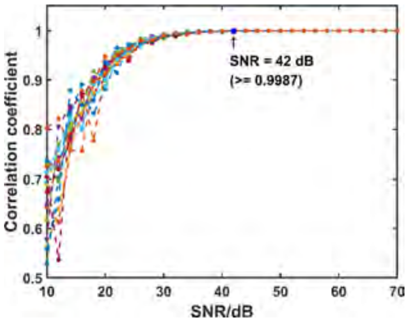

Figure 10. Variation of correlation coefficients with the SNR level of 16 randomly selected data.

Figure 11 shows the variation of average SNR with sensor electrode length in fluidized beds with different diameters. It can be seen that all average SNRs are higher than 43 dB, which ensures the sensor performance according to the above discussion. The average SNR is increasing with the increase of electrode length.

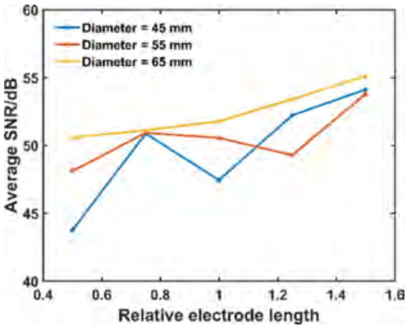

Figure 11. Variation of average SNR with relative electrode length in gas−solid fluidized beds of different diameters.

Next, fluidized bed characteristics measured by a sensor of different electrode lengths in fluidized beds with different diameters are studied.

4.2.1. Minimum Bubbling Velocity.

In this study, minimum bubbling velocity (U_{mb}) was measured by ECT and pressure drop of the fluidized bed simultaneously. Time-average solid concentration with its standard deviation and pressure drop of the fluidized bed were first measured with the increase of superficial velocity. Equations 20 and 21 show the time-averaged solid concentration and its standard deviation.

$$\overline{\beta} = \frac{1}{Q}\sum_{i=1}^{Q}\beta_i \tag{20}$$

Table 2. Fluidized Bed Particle (Alumina) Properties

material	bulk density (kg/cm^3)	particle size (μm)	Sauter particle diameter (μm)	solid fraction in fixed state	sphericity	minimum fluidization velocity (cm/s)	minimum bubbling velocity (cm/s)
alumina	1650	183−454	295	0.63	0.99	6.86	7.00

DOI: 10.1021/acs.iecr.9b03988
Ind. Eng. Chem. Res. 2019, 58, 21827−21841

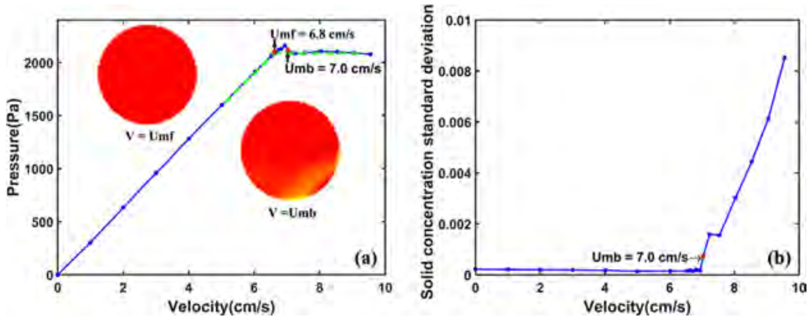

Figure 12. In a 55 mm diameter fluidized bed with an electrode length of 68.75 mm. (a) Minimum fluidization velocity and minimum bubbling velocity measured by pressure drop method and reconstructed images at above velocities. (b) Variation of solid concentration standard deviation with superficial velocity to determine minimum bubbling velocity.

$$\mathrm{STD} = \frac{1}{Q}\sum_{i=1}^{Q}(\beta_i - \bar{\beta})^2 \tag{21}$$

where β_i is the solid concentration of one frame in this work, and STD is the standard deviation of time-average solid concentration. Note that the sampling frequency is 70 Hz. U_{mb} is the point at which the standard deviation of solid concentration departs from the plateau. In the pressure drop measurement, U_{mb} is the point at which the decrease of pressure drop first occurs. Figure 12 shows the determination of U_{mb} in the 55 mm diameter fluidized bed with a 68.75 mm length electrode. It can be seen that the results of U_{mb} measured by ECT and pressure drop are consistent with each other, and the difference between minimum bubbling velocity and minimum fluidization velocity can be ignored because the bed material belongs to Geldart B particles.[32] The same findings can be observed in the measurements with other electrode lengths and fluidized bed diameters. More details about the methods could be found in the works of Huang et al.[31] and Agu et al.[13]

Figure 13 shows the results of U_{mb} measured by sensors with different electrode lengths in fluidized beds with different diameters. It shows that the sensor electrode length has a minor effect on the minimum bubbling velocity (or minimum fluidization velocity) measured.

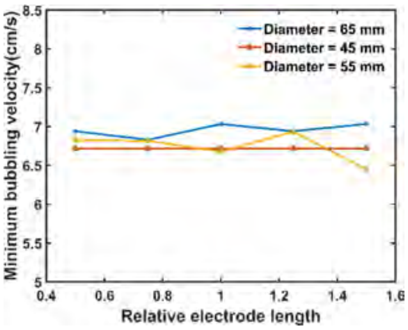

Figure 13. Minimum bubbling velocities measured by sensors with all electrode lengths and in fluidized beds with different diameters.

4.2.2. Average Solid Concentrations. The average solid concentration at a certain gas velocity is calculated by eq 20 as shown above. Figure 14 shows the average solid concentration as a function of superficial gas velocity in fluidized beds with different diameters using a sensor of different electrode lengths. The low limit of the studied velocity is set to the minimum bubbling velocity. It can be seen that the average solid concentration is gradually decreasing with the superficial gas velocity, while there are no obvious changes with varying electrode lengths in fluidized beds with different diameters.

4.2.3. Radial Solid Concentration Profile. Radial solid concentration profile can be used to correct fluidized bed simulation model and identify flow regime.[10] The radial solid concentration profile is measured by averaging samples according to radial locations in a time interval. Equation 22 computes the time-average solid concentration at the circle of radii r of the measurement zone

$$\bar{\beta}_r = \theta \cdot \frac{\sum_{j=1}^{c} \bar{g}_{rj}}{C} \tag{22}$$

where $\bar{\beta}_r$ represents the time-average solid concentration at the circle of radii r $(0 \leq r \leq R)$ in the measurement zone, R is the radius of the fluidized bed column, θ is the solid concentration of packed bed, c represents the number of pixels that are evenly sampled at the circle of radii r (i.e., 36 in our study), and $\bar{g}_{rj}$ represents the time-average normalized permittivity of the jth sampled pixel of the circle of radii r.

In this work, an appropriate time interval is first identified when the radial profile with this time interval does not change. Figure 15 shows the effect of sensor electrode length on radial solid concentration profile at different superficial gas velocities in a fluidized bed of 55 mm diameter. The nonuniform distribution of solid concentration indicates that there is bubble flowing through the measurement plane. It shows that the radial solid concentration profiles are similar for different sensor electrode lengths and different superficial gas velocities. It also shows that bubbles normally escape along the wall at a lower superficial velocity and approach the center at a higher superficial gas velocity, which is consistent with the results obtained by Makkawi and Wright.[10]

4.2.4. Bubble Size. Bubble size is a significant characteristic of a fluidized bed. In the following, we discuss the effect of sensor electrode length on bubble diameter measurements. First, quasi-3D images for the first 10 s of measurements, which are obtained by stacking a sequence of 2D images at a superficial velocity of 12.6 cm/s with different sensor electrode lengths in fluidized beds with different diameters, are presented in Figures 16−18. It can be seen that bubbles become more difficult to be detected as the sensor electrode length increases, which is consistent with the simulation results shown in Figure 7. It can also be seen that the fluidized bed diameter has a significant effect on bubble behavior. In the 45 mm diameter fluidized bed, a single bubble occupies almost all the cross

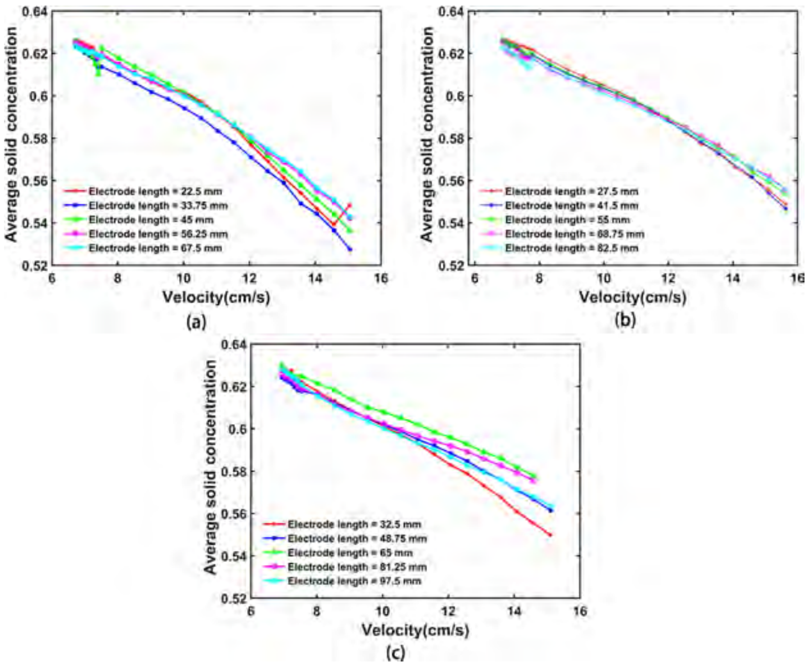

Figure 14. Average solid concentration as a function of superficial gas velocity with a sensor of different electrode lengths in fluidized beds with diameters of (a) 45, (b) 55, and (c) 65 mm.

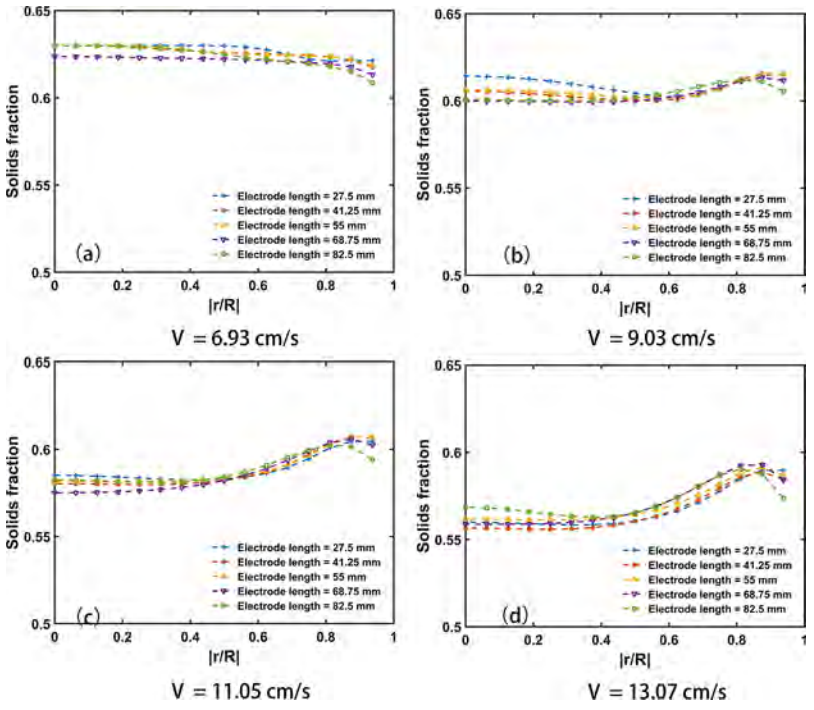

Figure 15. Radial solid concentration profile with different sensor electrode lengths in the 55 mm diameter fluidized bed at different superficial velocities. (a) 6.93 cm/s, (b) 9.03 cm/s, (c) 11.05 cm/s, and (d) 13.07 cm/s.

section and forms slugs, but this slugging fluidization decreases with the increase of fluidized bed diameter.

Next, quantitative comparisons were conducted by computing time-average bubble diameters to show the effect of sensor electrode length on bubble detection. Different methods have been used to estimate bubble diameters.[12,14,15] In this paper, the bubble diameter is obtained using a method described by Agu et al.[14] A constant threshold of solid concentration, that is, 0.315, is used to identify the bubbles and the emulsion phase considering the usage of excessively smoothed images.[12] It should be noted that the value of the threshold does not affect the trend shown in Figure 20.

Figure 19a shows the solid concentration time series obtained from the ECT images (as depicted in Figure 19b) measured in the 55 mm diameter fluidized bed with a sensor electrode length of 55 mm at a superficial velocity of 15 cm/s. As can be seen, when a bubble passes through the sensor, the solid concentration first decreases, demonstrating a valley as

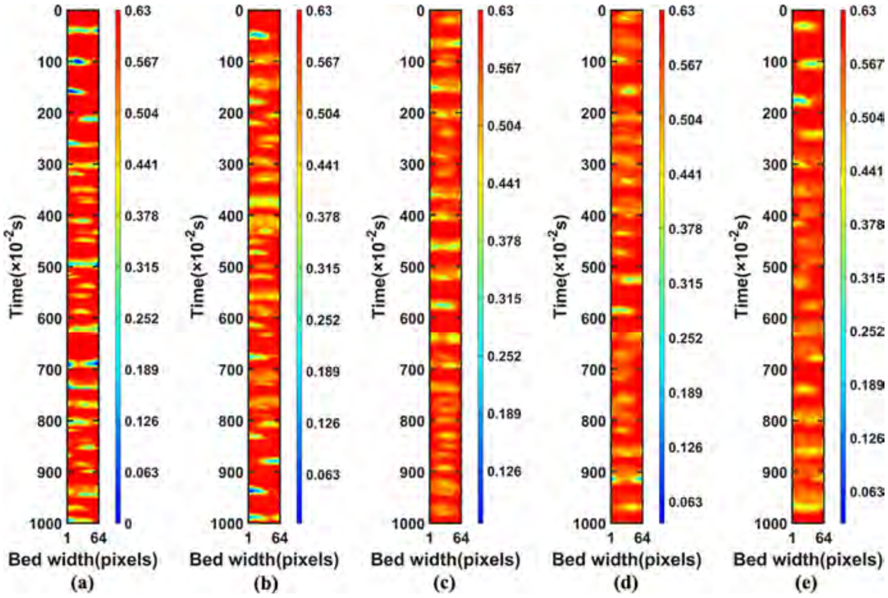

Figure 16. Quasi-3D images of solid concentration for the first 10 s of measurements in 45 mm diameter beds with a sensor of different electrode lengths at 12.6 cm/s. (a) 22.5 mm, (b) 33.75 mm, (c) 45 mm, (d) 56.25 mm, and (e) 67.5 mm.

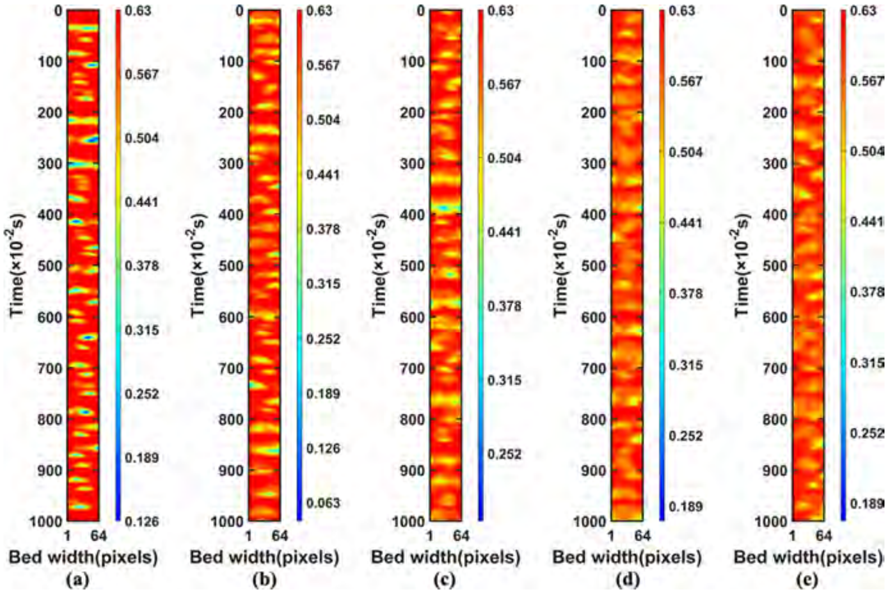

Figure 17. Quasi-3D images of solid concentration for the first 10 s of measurements in 55 mm diameter beds with a sensor of different electrode lengths at 12.6 cm/s. (a) 27.5 mm, (b) 41.25 mm, (c) 55 mm, (d) 68.75 mm, and (e) 82.5 mm.

the bubble is in the sensor center, and then increases when the bubble continuously passes through the sensor center. This is in accordance with the result of Agu et al.[14,18] Therefore, it is reasonable to use the valley of the solid concentration to identify the bubble diameter. Note that the solid concentration is related to the projected area of bubble, and we can obtain the bubble diameter by assuming the bubble is spherical

$$d_b = \frac{1}{T}\sum_{i}^{T}\sqrt{\frac{4A_{p,i}}{\pi}} \tag{23}$$

where d_b is the time-average bubble diameter and T is the number of valleys in the measurement of solid concentrations. The projected area $A_{p,i}$ of the ith bubble is

$$A_{p,i} = A\cdot(n_b/N) \tag{24}$$

where A is the cross-sectional area of the fluidized bed and n_b is the number of pixels occupied by the bubble. For more details, refer to Agu et al.[14]

Figure 20 shows the time-average bubble diameter for four different velocities in fluidized beds with three different diameters. It can be seen that bubble diameter in general decreases with the increase of sensor electrode length. The exception can be found at a superficial velocity of 14.6 cm/s in the 45 mm fluidized bed. A close check indicates that the bed, under this specified condition, forms slugs, and thus, the electrode length has little effect on the bubble diameter. This can be attributed to the fact that a sensor with shorter length could approach the real bubble size accurately. The use of longer electrodes would underestimate the bubble size, as

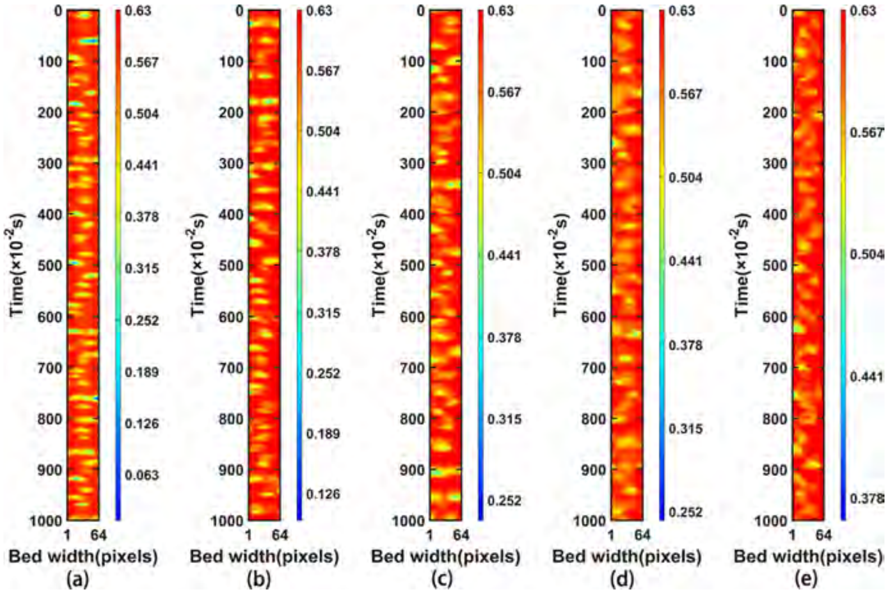

Figure 18. Quasi-3D images of solid concentration for the first 10 s of measurements in 65 mm diameter beds with a sensor of different electrode lengths at 12.6 cm/s. (a) 32.5 mm, (b) 48.75 mm, (c) 65 mm, (d) 81.25 mm, and (e) 97.5 mm.

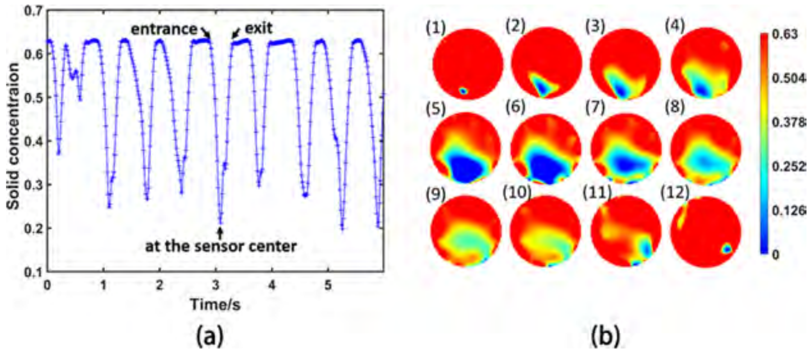

Figure 19. Solid concentration time series obtained from ECT images measured in the 55 mm diameter fluidized bed with a sensor electrode length of 55 mm at a superficial velocity of 15 cm/s: (a) solid concentration time series and (b) ECT images when a bubble passes through the sensor.

shown in Figures 16−18, which agrees well with the simulation results as shown in Figure 7.

Bubble diameters from empirical correlation[33] are also shown in Figure 20. It can be seen that the discrepancy between ECT measurements and the correlation decreases and further disappears with the increase of superficial velocity. The prominent discrepancy at lower superficial velocity (smaller than $1.5U_{mb}$) may be related to the distinct difference of fluidized bed configurations or the low resolution of ECT measurements (normally 5−10% of the vessel diameter).[15] Besides, the correlation-predicted results are consistent with ECT measurements at superficial velocities higher than $1.5U_{mb}$, which indeed confirms the aforementioned analysis. More details might be expected by directly coupling the electrostatic field simulations and fluidized bed CFD simulations.

4.2.5. Spectral Analysis and Regime Transition. The dominant frequency obtained by spectral analysis is regarded as the frequency that has the maximum module in the spectrum distribution, which reflects bubble movements in fluidized beds.[17] The spectrum distribution in this work is computed using FFT algorithm. According to the work of Li et al.,[16] a broad-band spectrum is observed in bubble regime, and there is no obvious peak of frequency module. Therefore, the dominant frequencies obtained in this regime have irregular characteristics. With the increase of superficial gas velocity, the fluidized bed can transit to a single bubble or slugging regime depending on whether the bubble size is larger than half of the bed diameter. In this case, a narrow spectrum distribution with a sharp peak is formed, and thus, a prominent dominant frequency of fluidized bed can be obtained, which can be used to distinguish bubble regime and single or slugging regime. Figure 21 shows two different spectrum distributions at different superficial velocities as an example. Figure 21a has a broad-band spectrum with no prominent dominant frequency, while Figure 21b has a narrow band with a prominent dominant frequency. Fluidization at these superficial velocities can be regarded as in the bubble regime and slugging (or single bubble) regime, respectively.

Figure 22 shows the variation of dominant frequency with superficial velocity from minimum bubbling velocity in fluidized beds with different diameters. It can be seen that there exist two different regimes based on the amplitude of the dominant frequency. According to Li et al.,[16] the marked line can be regarded as the transition from bubble regime to single bubble or slugging regime. As can be seen from Figure 22 that the transition velocity increases with the fluidized bed

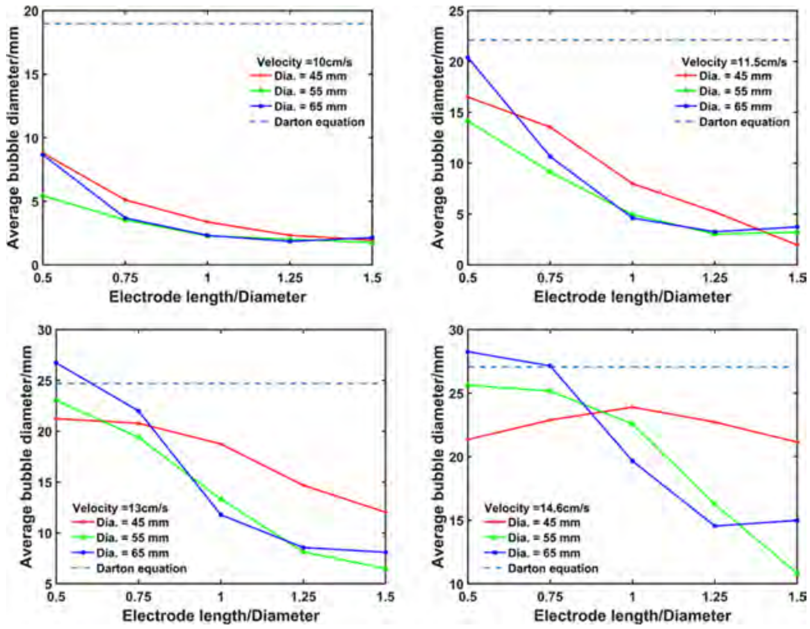

Figure 20. Bubble diameters measured by a sensor with different electrode lengths at four superficial velocities in fluidized beds with three different diameters and comparisons with the correlation by Darton et al.[33]

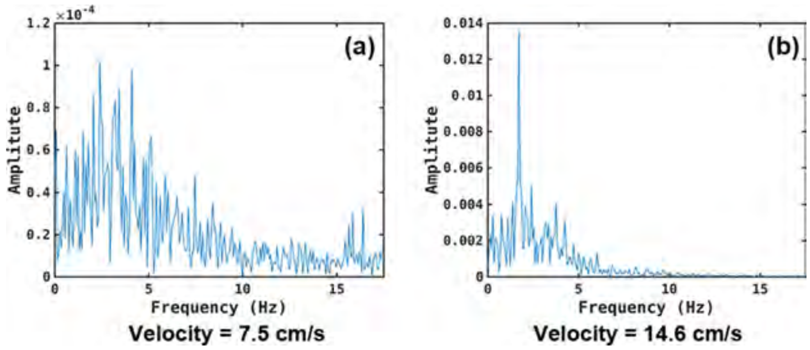

Figure 21. Spectrum distributions measured by a sensor with an electrode length of 68.75 mm in a fluidized bed of 55 mm diameter. (a) Bubble regime. (b) Single bubble regime.

diameter, which can be explained as slugging is hard to happen in fluidized beds with larger diameters. It can be anticipated that the electrode length has a minor effect on this transition velocity based on one-plane ECT sensor (as shown in Figure 22) measurements. However, obtaining an accurate slugging velocity might require a two-plane ECT sensor.[10,13] In the single bubble or slugging regime, it can be seen that the dominant frequency decreases with the superficial gas velocity irrespective of electrode length. A higher dominant frequency is found for the sensor with shorter electrode length. When the gas velocity increases, the dominant frequencies obtained by sensors with different electrode lengths coincide with each other. It can be found from the reconstructed images by ECT measurements that the single bubble passes the sensor rhythmically and the bubble size increases with the increase of superficial velocity. In fact, the sensor with shorter electrode length has smaller detecting zone, which could detect smaller bubbles and approach a real bubble movement frequency in the fluidized bed. The sensor with longer electrode could only measure larger bubbles as shown in Figures 16–18, which in turn leads to a decrease in the measured frequency. This can explain the variation of dominant frequency with the change of superficial gas velocity in the 65 mm diameter fluidized bed as shown in Figure 22c. Here, the dominant frequencies are not consistent with each other for the superficial velocity internal used in the measurements because the bubble size is smaller than the electrode length. This can be further studied by coupling the fluidized bed CFD simulations with electrostatic field simulations for time being.

5. CONCLUSIONS

This study investigated the effect of ECT sensor electrode length on fluidized bed measurements by simulations and experiments. Numerical results of sensitivity distribution along the axial position of the sensor were obtained, showing the similarity of sensitivity distribution contour and variation of sensitivity distribution intensity with the distance to electrode center. As a general rule, sensitivity distribution contours are similar to each other inside the electrode cross section, and the sensitivity distribution intensity is the maximum in the electrode center and decreases with the axial distance to electrode center, finally dropping to zero at a point which depends on the specific electrode length and is outside the electrode axial edge. Results of placing the same phantoms at

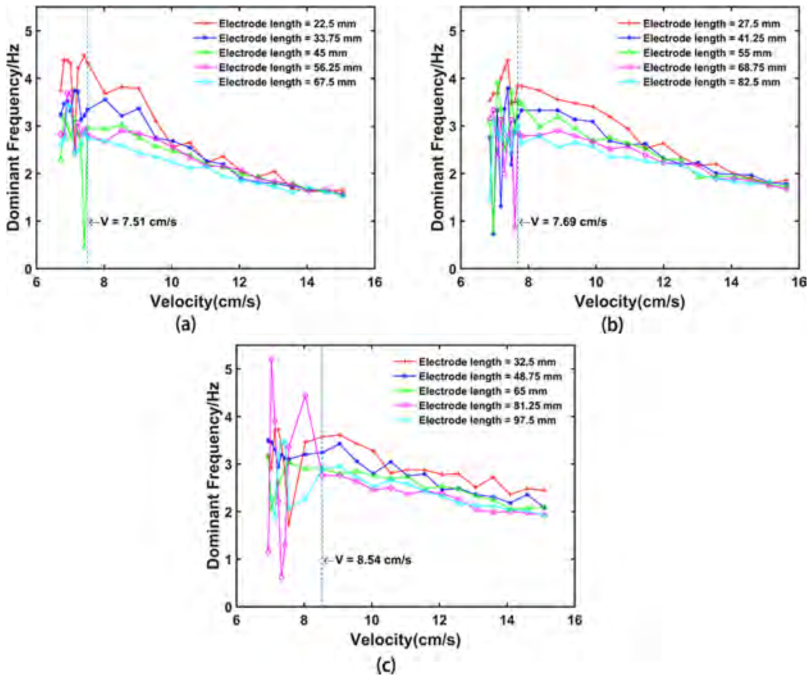

Figure 22. Variation of dominant frequency with superficial gas velocity in fluidized beds with three diameters and with different sensor electrode lengths. (a) 45 mm, (b) 55 mm, and (c) 65 mm.

different axial locations of the sensor confirmed this conclusion.

Considering the effect of sensor axial position on ECT measurements, experiments were conducted in fluidized beds with three different diameters (45, 55, and 65 mm) to study the effect of sensor electrode length on fluidized bed measurements. The ratios of sensor electrode length to fluidized bed inner diameter were set to 0.5, 0.75, 1, 1.25, and 1.5 in each fluidized bed. A series of measurements were taken with different electrode lengths at the same superficial velocity. The characteristics of the fluidized bed, such as the minimum bubbling velocity, the relationship between average solid concentration and superficial velocity, the radial solid concentration profile at different velocities, the dominant frequency of fluidized bed, and bubble characteristic, were compared to show the effect of electrode length on fluidized bed measurements. The results show that the sensor electrode length has some influence on fluidized bed measurements, especially for bubble diameter detection and dominant frequency of fluidized bed at low superficial velocity. More specifically, the bubble diameter is decreasing with the increase of electrode length. At a low superficial velocity in a single bubble or slugging regime, a fluidized bed with smaller electrode length has higher frequency. Except for these two parameters closely related to the bubble size, electrode length has no influence on the measurements of other fluidization characteristics such as the minimum bubbling velocity, the transition velocity from the bubble regime to the single bubble or slugging regime, and the radial solid concentration profile.

Based on the above results, it is recommended that, when an ECT sensor is designed for measuring bubble size in fluidized beds, its electrode length should be as small as possible considering that the average SNR is beyond a benchmark. For example, the SNR should be higher than 42 dB if the correlation coefficient between the reconstructed images with noised signals and that without noise is set to be 0.9987.

■ ASSOCIATED CONTENT

Ⓢ Supporting Information

The Supporting Information is available free of charge on the ACS Publications website at DOI: 10.1021/acs.iecr.9b03988.

> Procedure of dividing measurement zone of a circular sensor into 3228 pixels; effect of pixel number on image reconstructions by the same capacitance vectors; and lowest correlation coefficient which is not less than 0.990 of 16 randomly chosen data on different SNR levels (PDF)

■ AUTHOR INFORMATION

Corresponding Author

*E-mail: maoye@dicp.ac.cn.

ORCID

Qiang Guo: 0000-0002-8857-1961
Mao Ye: 0000-0002-7078-2402
Zhongmin Liu: 0000-0002-7999-2940

Notes

The authors declare no competing financial interest.

■ ACKNOWLEDGMENTS

The authors are grateful to the National Key Research and Development Program of China (grant no. 2018YFB0604904) and the National Natural Science Foundation of China (grant no. 91834302).

■ ABBREVIATION

ECT electrical capacitance tomography

■ NOMENCLATURE

S	normalized sensitivity matrix
g	normalized permittivity
S^*	sensitivity matrix

E	electrode field strength, V/m
V	potential difference, V
M	number of electrode pairs, 66
N	number of pixels in measurement zone, 3228
C	capacitance
e	error vector
P	function operator
R	radius of the fluidized bed column, 22.5, 27.5, and 32.5 mm
s	pixel area
q	quantity of electric charge, C
Q	number of frames of each measurement, 20 000
STD	standard deviation of average solid concentration
d_b	average bubble diameter, mm
T	number of valley in the measurement series
$A_{p,i}$	projected bubble area of the ith bubble, mm^2
A	cross-sectional area of fluidized bed, mm^2
n_b	number of pixels occupied by bubble.

GREEK SYMBOLS

λ	normalized capacitance
α	optimal step length
β	solid concentration
θ	solid concentration of a packed bed, 0.63
ε	relative permittivity
ϕ	electric potential, V
Γ	electrode
r	correlation coefficient
SNR	signal-to-noise ratio, dB
U_{mb}	minimum bubbling velocity, cm/s
c	number of pixels sampled from radii r circle, 36

SUBSCRIPT

H	high calibration state
L	low calibration state
0	initial estimation
S	shield and earthed axial shield electrode.
r	radial distribution
b	nubble in fluidized bed

SUPERSCRIPT

^	reconstructed value
-	average value

REFERENCES

(1) Tian, P.; Wei, Y.; Ye, M.; Liu, Z. Methanol to Olefins (MTO): From Fundamentals to Commercialization. *ACS Catal.* **2015**, *5*, 1922.

(2) Bai, P.; Etim, U. J.; Yan, Z.; Mintova, S.; Zhang, Z.; Zhong, Z.; Gao, X. Fluid catalytic cracking technology: current status and recent discoveries on catalyst contamination. *Catal. Rev.* **2018**, *61*, 333.

(3) Basu, P. Combustion of coal in circulating fluidized-bed boilers: a review. *Chem. Eng. Sci.* **1999**, *54*, 5547.

(4) Werther, J. Measurement techniques in fluidized beds. *Powder Technol.* **1999**, *102*, 15.

(5) Hage, B.; Werther, J.; Narukawa, K.; Mori, S. Capacitance probe measurement technique for local particle volume concentration in circulating fluidized bed combustors. *J. Chem. Eng. Jpn.* **1996**, *29*, 594.

(6) Wiesendorf, V.; Werther, J. Capacitance probes for solids volume concentration and velocity measurements in industrial fluidized bed reactors. *Powder Technol.* **2000**, *110*, 143.

(7) Xu, G.; Liang, C.; Chen, X.; Liu, D.; Xu, P.; Shen, L.; Zhao, C. Investigation on dynamic calibration for an optical-fiber solids concentration probe in gas-solid two-phase flows. *Sensors* **2013**, *13*, 9201.

(8) Rüdisüli, M.; Schildhauer, T. J.; Biollaz, S. M. A.; Ruud van Ommen, J. Bubble characterization in a fluidized bed by means of optical probes. *Int. J. Multiphase Flow* **2012**, *41*, 56.

(9) van Ommen, J. R.; Mudde, R. F. Measuring the Gas-Solids Distribution in Fluidized Beds -- A Review. *Int. J. Chem. React. Eng.* **2008**, *6*. DOI: 10.2202/1542-6580.1796

(10) Makkawi, Y. T.; Wright, P. C. Fluidization regimes in a conventional fluidized bed characterized by means of electrical capacitance tomography. *Chem. Eng. Sci.* **2002**, *57*, 2411.

(11) Qiu, G.; Ye, J.; Wang, H.; Yang, W. Investigation of flow hydrodynamics and regime transition in a gas−solids fluidized bed with different riser diameters. *Chem. Eng. Sci.* **2014**, *116*, 195.

(12) Chandrasekera, T. C.; Li, Y.; Moody, D.; Schnellmann, M. A.; Dennis, J. S.; Holland, D. J. Measurement of bubble sizes in fluidised beds using electrical capacitance tomography. *Chem. Eng. Sci.* **2015**, *126*, 679.

(13) Agu, C. E.; Tokheim, L.-A.; Eikeland, M.; Moldestad, B. M. E. Determination of onset of bubbling and slugging in a fluidized bed using a dual-plane electrical capacitance tomography system. *Chem. Eng. J.* **2017**, *328*, 997.

(14) Agu, C. E.; Pfeifer, C.; Eikeland, M.; Tokheim, L.-A.; Moldestad, B. M. E. Models for Predicting Average Bubble Diameter and Volumetric Bubble Flux in Deep Fluidized Beds. *Ind. Eng. Chem. Res.* **2018**, *57*, 2658.

(15) Li, X.; Jaworski, A. J.; Mao, X. Bubble size and bubble rise velocity estimation by means of electrical capacitance tomography within gas-solids fluidized beds. *Measurement* **2018**, *117*, 226.

(16) Li, X.; Jaworski, A. J.; Mao, X. Comparative study of two non-intrusive measurement methods for bubbling gas-solids fluidized beds: Electrical capacitance tomography and pressure fluctuations. *Flow Meas. Instrum.* **2018**, *62*, 255.

(17) Agu, C. E.; Tokheim, L.-A.; Eikeland, M.; Moldestad, B. M. E. Improved models for predicting bubble velocity, bubble frequency and bed expansion in a bubbling fluidized bed. *Chem. Eng. Res. Des.* **2019**, *141*, 361.

(18) Agu, C. E.; Ugwu, A.; Pfeifer, C.; Eikeland, M.; Tokheim, L.-A.; Moldestad, B. M. E. Investigation of Bubbling Behavior in Deep Fluidized Beds at Different Gas Velocities using Electrical Capacitance Tomography. *Ind. Eng. Chem. Res.* **2019**, *58*, 2084.

(19) Yang, W. Design of electrical capacitance tomography sensors. *Meas. Sci. Technol.* **2010**, *21*, 042001.

(20) Yang, W. Q.; Peng, L. Image reconstruction algorithms for electrical capacitance tomography. *Meas. Sci. Technol.* **2003**, *14*, R1.

(21) Hua, Y.; FuQun, S.; Hui, X.; Shi, W. Three-dimensional analysis of electrical capacitance tomography sensing fields. *Meas. Sci. Technol.* **1999**, *10*, 717.

(22) Peng, L.; Ye, J.; Lu, G.; Yang, W. Evaluation of effect of number of electrodes in ECT sensors on image quality. *IEEE Sens. J.* **2011**, *12*, 1554.

(23) Peng, L.; Mou, C.; Yao, D.; Zhang, B.; Xiao, D. Determination of the optimal axial length of the electrode in an electrical capacitance tomography sensor. *Flow Meas. Instrum.* **2005**, *16*, 169.

(24) Sun, J.; Yang, W. Fringe effect of electrical capacitance and resistance tomography sensors. *Meas. Sci. Technol.* **2013**, *24*, 074002.

(25) Tian, W.; Sun, J.; Ramli, M. F.; Yang, W. Effect of electrode-to-gap ratio on electrical capacitance tomography images. *International Conference on Imaging Systems and Techniques (IST), Chania, Greece*; IEEE: Washington, DC, Oct 4−6, 2016; p 294.

(26) Mao, M.; Ye, J.; Wang, H.; Yang, W. Evaluation of Excitation Strategies for 3D ECT in Gas-solids Flow Measurement. *IEEE Sens. J.* **2016**, *16*, 8523.

(27) Olmos, A. M.; Carvajal, M. A.; Morales, D. P.; García, A.; Palma, A. J. Development of an Electrical Capacitance Tomography system using four rotating electrodes. *Sens. Actuators, A* **2008**, *148*, 366.

(28) Liu, S.; Fu, L.; Yang, W. Q. Optimization of an iterative image reconstruction algorithm for electrical capacitance tomography. *Meas. Sci. Technol.* **1999**, *10*, L37.

(29) Guo, Q.; Meng, S.; Wang, D.; Zhao, Y.; Ye, M.; Yang, W.; Liu, Z. Investigation of gas-solid bubbling fluidized beds using ECT with a modified Tikhonov regularization technique. *AIChE J.* **2018**, *64*, 29.

(30) Sathiyamoorthy, D.; Horio, M. On the influence of aspect ratio and distributor in gas fluidized beds. *Chem. Eng. J.* **2003**, *93*, 151.

(31) Huang, K.; Meng, S.; Guo, Q.; Ye, M.; Shen, J.; Zhang, T.; Yang, W.; Liu, Z. High-temperature electrical capacitance tomography for gas−solid fluidised beds. *Meas. Sci. Technol.* **2018**, *29*, 104002.

(32) Geldart, D. Types of gas fluidization. *Powder Technol.* **1973**, *7*, 285.

(33) Darton, R. C.; Lanauze, R. D.; Davidson, J. F.; Harrison, D. Bubble growth due to coalescence in fluidized beds. *Trans. Inst. Chem. Eng.* **1977**, *55*, 274.